Collisional Processes at Low Densities in Magnetic Mirror Systems

A. H. Futch, C. C. Damm, J. H. Foote, A. L. Gardner, and J. Killeen

Citation: Physics of Fluids (1958-1988) **14**, 1542 (1971); doi: 10.1063/1.1693641
View online: http://dx.doi.org/10.1063/1.1693641
View Table of Contents: http://scitation.aip.org/content/aip/journal/pof1/14/7?ver=pdfcov
Published by the AIP Publishing

Collisional Processes at Low Densities in Magnetic Mirror Systems

A. H. Futch, C. C. Damm, J. H. Foote, A. L. Gardner,* and J. Killeen
Lawrence Radiation Laboratory, University of California, Livermore, California 94550
(Received 12 October 1970; final manuscript received 31 March 1971)

The study of collisional processes in plasmas produced by neutral-atom injection into magnetic mirror fields is described. The emphasis is on the many collisional processes which occur as the plasma density increases. Experimental and theoretical results are given. The experimental results are discussed first in terms of a simple model which assumes a Maxwellian electron distribution and a monoenergetic ion component of much higher energy. Analytical solutions may be obtained for this model. Also presented is a more complete theory employing two time-dependent Fokker–Planck equations to describe the behavior of the electron and ion distribution functions. Both models are in good agreement with measured values of the electron temperature and plasma potential. The equilibrium values of these two quantities are found to vary as the $\frac{2}{3}$ power of the ratio of the plasma density to the background-gas density.

I. INTRODUCTION

In plasmas contained by "open-ended" or magnetic mirror systems, particles may be lost from the system by collisions that scatter the particles into the mirror loss cones. Chandrasekhar[1] has considered similar scattering effects for stellar collisions. Spitzer,[2] by extending Chandrasekhar's theory to an ionized plasma, has shown that the characteristic time for loss of a charged particle by scattering is proportional to the $\frac{3}{2}$ power of the particle energy. Therefore, unless the charge species of the plasma have the same energy, the scattering loss times generally will be different; and an electrostatic potential then develops to balance the loss rates, resulting in approximate charge neutrality.

In magnetic mirror systems where the ion energy is large compared with the mean electron energy a positive plasma potential develops, retarding the electron loss but increasing the ion loss. In an early investigation, Kaufman[3] assumed that the magnetic field configuration could be approximated by a "square well." He found that electrons either were confined or had their loss cones reduced by a positive potential. For ions, however, the loss cone was increased; and a minimum energy was found to exist for which there was no confinement due to expulsion by the positive potential. Other authors[4–7] have included a variation of the electrostatic potential along the direction of the magnetic field lines, instead of starting from Kaufman's "square-well" assumption.

To describe the electron temperature and electrostatic potential of a plasma produced by neutral-atom injection into a magnetic mirror field, additional source and loss terms are necessary. A simple model including these extra terms was presented in an earlier paper by three of the present authors.[8] This model, which assumes a Maxwellian electron distribution and a monoenergetic ion component of a much higher energy, employs two buildup equations (first-order differential equations) to describe the collisional processes affecting the ion and electron densities. The success of this approach in describing the measured electron temperature and plasma potential has led to refinement of the original model to include, for the previous approximation $\exp(-e\phi/kT_e)$, the substitution of an exact expression for the fraction of electrons that have energy greater than $e\phi$. In addition, the ion scattering term is not neglected now, and the initial electron energy is assumed to have a value other than zero.

If the distribution function for a particular plasma species is expected to change in an unknown way, then the ordinary differential equation describing the density of that species must be replaced by a partial differential equation describing the distribution function of that species in velocity space. The most suitable mathematical description comes from the Fokker–Planck equation. This is because the dominant mechanism for energy transfer among the particles is by long-range Coulomb interactions. The Fokker–Planck equation for the distribution functions of several species of particles, where the two-body force is an inverse square law, has been derived by Rosenbluth, MacDonald, and Judd.[9] This equation has been used by many authors for numerical calculations of end-loss rates.[7,10–14]

In the present work, the Fokker–Planck equation serves as a tool for understanding the time dependence of plasma parameters such as density, electron temperature, electrostatic potential, and the distribution functions. Two time-dependent Fokker–Planck equations are employed to describe the behavior of the electron and ion distribution functions. The Fokker–Planck equations and the method for obtaining numerical solutions have previously been described.[15]

The theory describing the collisional processes in a plasma produced by neutral-atom injection in a magnetic mirror field is described in Sec. II, where it is discussed in terms of buildup equations for the density of the ion and electron plasma components and also in terms of the corresponding Fokker–Planck equations for the distribution functions. In Sec. III, the experimental measurements of the plasma potential ϕ and the electron temperature T_e are described. The plasma potential measurements were obtained by monitoring the parallel energy of the slow ions leaving the plasma

along the magnetic axis.[16] Relative measurements of the electron temperature were obtained from the amplitude of microwave radiation emitted at the electron cyclotron frequency.

In Sec. IV, we compare theoretical calculations and experimental measurements. Some additional results on collisional broadening of the ion distribution function are discussed in Sec. V. All experimental and theoretical results in this paper assume the plasma ions to be protons. Section VI contains some concluding remarks.

II. THEORY

A. Simple Model Employing First-Order Differential Equations

The electron temperature T_e and plasma potential ϕ of a plasma produced by neutral-atom injection into a magnetic mirror field may be obtained by considering the buildup equations for the ion density n_i and the electron density n_e of the plasma. These equations, which assume a Maxwellian electron distribution and a monoenergetic ion component, describe the collisional processes in the plasma in terms of cross sections averaged over the relative velocities of the interacting particles.

The energetic neutral-atom beam I is trapped by Lorentz ionization of excited neutral atoms produced by charge-exchange collisions in a gas or vapor. Other trapping processes include ionizing collisions with the background gas and with previously trapped ions and electrons. Cross sections for these processes are represented by σ_t^n, σ_t^i, and σ_t^e, respectively. Cross sections for ion losses by charge-exchange collisions and by scattering into the mirror loss cone are represented by σ_{cx} and σ_s^i. The cross section for electrons lost by scattering into the loss cone is σ_s^e. Electrons are also formed by ionizing collisions of ion and electrons with the background gas; these collisions are described by the cross sections σ_i^i and σ_i^e, respectively.

For a background-gas density n_0 the differential equations for the ion and electron density become

$$\frac{dn_i}{dt}=\frac{If^*}{V}+\frac{IL}{V}n_0\left(\frac{\overline{\sigma_t^n v_r}}{v}\right)+n_i\left(\frac{IL}{Vv}(\overline{\sigma_t^i v_r}+\overline{\sigma_t^e v_r})-n_0\sigma_{cx}v\right)-n_i^2\overline{\sigma_s^i v}, \quad (1)$$

$$\frac{dn_e}{dt}=\frac{If^*}{V}+\frac{IL}{V}n_0\left(\frac{\overline{\sigma_t^n v_r}}{v}\right)+n_e\left(\frac{IL}{Vv}(\overline{\sigma_t^i v_r}+\overline{\sigma_t^e v_r})+n_0(\sigma_i^i v+\overline{\sigma_i^e v_e})\right)-n_e^2(\overline{\sigma_s^e v_e})F\left(\frac{e\phi}{kT_e}\right), \quad (2)$$

where $F(e\phi/kT_e)$ is the fraction of electrons with energy greater than $e\phi$. The beam velocity, the relative velocity between colliding particles, and the electron velocity are given by v, v_r, and v_e, respectively. The path length of the beam through the plasma volume V is given by L, and the fraction of the beam that is ionized by the Lorentz force of the magnetic field is given by f^*. Throughout this paper, n_0 refers to the number of molecules per cubic centimeter. We assume the background gas to be hydrogen.

In Eqs. (1) and (2), we assumed quasineutrality (i.e., $n_i \approx n_e$) and neglected the charge exchange of the trapped ions with the neutral beam. This latter process, which replaces one hot ion by another, has no net effect on spatially independent equations such as Eqs. (1) and (2). It has been shown that charge exchange of the trapped ions with the neutral beam may be regarded as a diffusion of the ions across the magnetic field lines for a finite plasma.[8] For a distribution function which is not monoenergetic, this process tends to sharpen the trapped distribution.[17]

The rate at which electrons leave the plasma by Coulomb scattering into the loss cones may be estimated by saying that the only effect of the plasma potential ϕ is to eliminate the loss of electrons with energy less than $e\phi$. The fraction of scattered electrons having sufficient energy to escape over the potential barrier is

$$F\left(\frac{e\phi}{kT_e}\right)=1+\frac{2}{\pi^{1/2}}\left(\frac{e\phi}{kT_e}\right)^{1/2}\exp\left(-\frac{e\phi}{kT_e}\right)-\Phi\left(\frac{e\phi}{kT_e}\right), \quad (3)$$

where $\Phi(e\phi/kT_e)$ is the probability integral. Combining (3) with the scattering rate gives the last term of Eq. (2).

In the following analysis, we make the additional assumption that the plasma "growth rate" is slow compared with the collisional relaxation times of the electrons; i.e., the electron temperature and scattering rates are in quasiequilibrium with the existing plasma density. The electrical neutrality of a plasma implies that

$$\frac{dn_i}{dt}\approx\frac{dn_e}{dt}. \quad (4)$$

By equating Eqs. (1) and (2), we obtain

$$-n_i n_0\sigma_{cx}v-n_i^2\overline{\sigma_s^i v}=n_e n_0(\sigma_i^i v+\overline{\sigma_i^e v_e})-n_e^2(\overline{\sigma_s^e v_e})F(e\phi/kT_e). \quad (5)$$

Rearranging terms and equating n_i to n_e, we have

$$F\left(\frac{e\phi}{kT_e}\right)=\frac{n_0(\sigma_i^i v+\overline{\sigma_i^e v_e}+\sigma_{cx}v)}{n_i(\overline{\sigma_s^e v_e})}+\frac{\overline{\sigma_s^i v}}{\overline{\sigma_s^e v_e}}. \quad (6)$$

A plasma contained in a magnetic mirror field is expected to generate a positive electrostatic potential if the ion energy is greater than the electron energy. Since the positive potential restricts electron escape,

the electrons are held by the plasma until they receive sufficient energy from collisions with the energetic ions to overcome the plasma potential. The electrons may then escape by scattering into the mirror loss cone. Thus, the plasma potential may be estimated by dividing the average energy the electrons obtain before escaping the plasma by the electronic charge; $e\phi$ is approximately equal to the average energy of the escaping electrons.

If the ion energy W is much greater than kT_e, the energy transfer rate from the protons to the electrons[18] is

$$\frac{dW}{dt}=\frac{1.8\times10^{-12}n_iW}{(kT_e)^{3/2}}, \tag{7}$$

where the ion energy and kT_e are expressed in keV. From Eq. (5), the average lifetime of an electron is given by

$$\tau_e=[n_0(\sigma_i{}^iv+\overline{\sigma_i{}^ev_e}+\sigma_{cx}v)+n_i\overline{\sigma_e{}^iv}]^{-1}. \tag{8}$$

Therefore the average energy of the escaping electrons is

$$e\phi=\frac{dW}{dt}\tau_e+E_0, \tag{9}$$

or

$$e\phi=\frac{1.8\times10^{-12}n_iW}{(kT_e)^{3/2}[n_0(\sigma_i{}^iv+\overline{\sigma_i{}^ev_e}+\sigma_{cx}v)+n_i\overline{\sigma_e{}^iv}]}+E_0, \tag{10}$$

where E_0 is the energy with which the electrons are born. Equations (6) and (10) may be solved by an iterative process for the two unknowns ϕ and T_e.

If $F(e\phi/kT_e)$ is approximated by

$$\exp(-e\phi/kT_e) \tag{11}$$

and the initial electron energy E_0 is neglected, then the following closed-form expressions for kT_e and $e\phi$ are obtained:

$$kT_e=\left(\frac{-1.8\times10^{-12}n_iW}{[n_0(\sigma_i{}^iv+\overline{\sigma_i{}^ev_e}+\sigma_{cx}v)+n_i\overline{\sigma_e{}^iv}]\ln K(n_0,n_i)}\right)^{2/5}, \tag{12}$$

$$e\phi=-kT_e\ln K(n_0,n_i), \tag{13}$$

where

$$K(n_0,n_i)=\left(\frac{n_0(\sigma_i{}^iv+\overline{\sigma_i{}^ev_e}+\sigma_{cx}v)}{n_i(\overline{\sigma_e{}^ev_e})}+\frac{\overline{\sigma_e{}^iv}}{\overline{\sigma_e{}^ev_e}}\right). \tag{14}$$

The foregoing state that the electron temperature and electrostatic potential are slowly varying functions of the ion density, i.e.,

$$T_e\propto(n_i/n_0)^{2/5} \tag{15}$$

and

$$\phi\propto(n_i/n_0)^{2/5} \tag{16}$$

if we neglect the dependence given by the logarithmic factor.

B. Fokker–Planck Equations

Replacing the two first-order differential equations of Sec. IIA with time-dependent Fokker–Planck equations for the ion and electron distribution functions enables us to solve a wider range of problems. Of particular interest are problems with time dependence and those which involve a change in the ion distribution function. The calculated electron distribution functions were always found to be Maxwellian in nature for densities above 10^7 particles/cm^3.

As noted, the Fokker–Planck equation for an inverse-square force is derived in the paper of Rosenbluth, MacDonald, and Judd.[9] In Eq. (31) of that paper, the result is given in spherical polar coordinates in

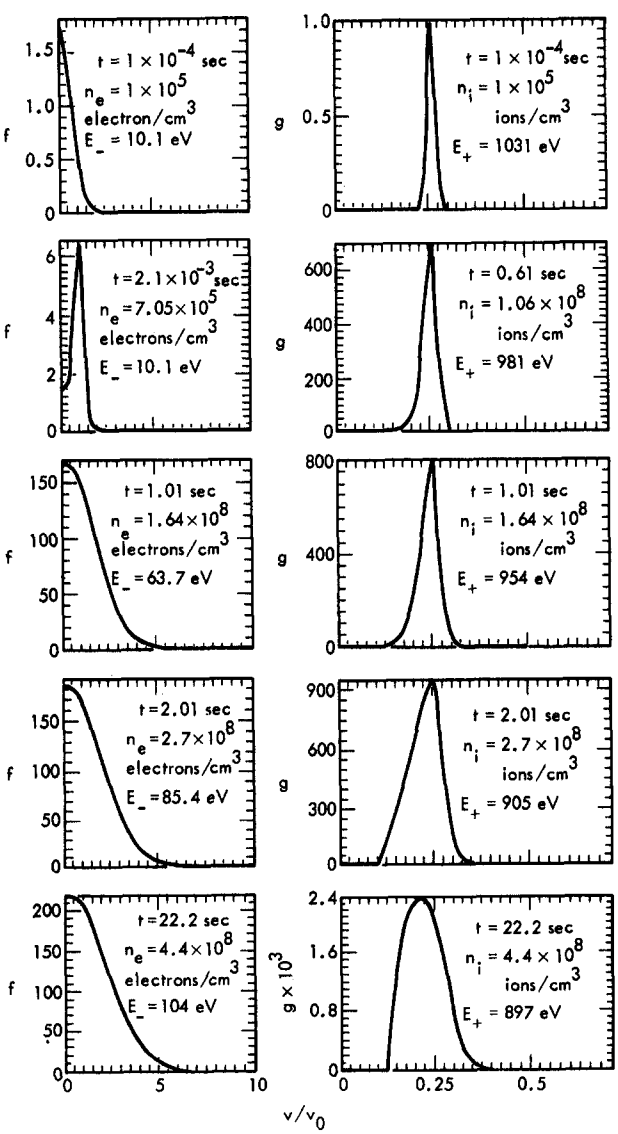

FIG. 1. Electron and ion distribution functions as a function of v/v_0 for various times. The initial electron energy is 10 eV, and the initial ion energy is 1 keV.

velocity space, assuming azimuthal symmetry. We further assume that the distribution functions are isotropic in velocity space; i.e., there is no θ dependence. The functions depend only on v, the magnitude of the velocity, and t, the time. We have also modified the Fokker–Planck equation to include source and loss terms, so that for both the electron and ion distribution functions the equation takes the form

$$\frac{\partial f_a}{\partial t} = A\frac{\partial^2 f_a}{\partial v^2} + B\frac{\partial f_a}{\partial v} + Cf_a + D. \qquad (17)$$

The ion-loss term includes both Coulomb scattering into the loss cone and charge exchange. Additional discussion of this equation is given in the Appendix.

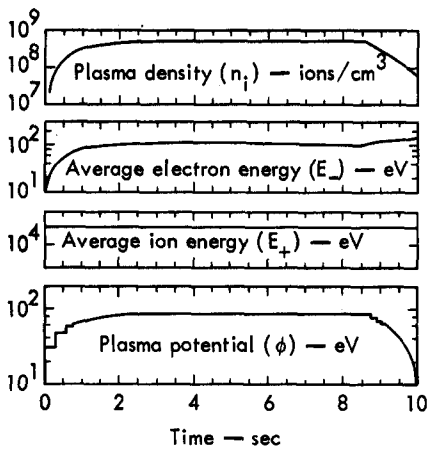

FIG. 2. Plasma parameters n_i, E_-, E_+, and ϕ as a function of time, for an injection energy of 15 keV. The beam is turned off at a time corresponding to approximately 8.5 (dimensionless units).

The numerical code we employed is capable of providing graphical output plus numerical data. Figure 1 shows typical ion and electron distributions as a function of the normalized velocity v/v_0 for various times during the buildup process. In this case, a 1-keV neutral beam consisting of 6.2×10^{15} atoms/sec was assumed to have a Lorentz trapping fraction, f^*, equal to 4.2×10^{-5}. The plasma volume V was 7.5 liters. Parameters such as plasma density (n_i), average electron energy (E_-), average ion energy (E_+), and the plasma potential (ϕ) also can be plotted as a function of time, as shown in Fig. 2. The results here are for a 15-keV plasma reaching equilibrium between trapping and loss processes at approximately 5×10^8 ions/cm^3.

III. EXPERIMENTAL METHOD

A. Measurement of the Plasma Potential

In the Livermore neutral-injection experiment Alice, the potential of the plasma was determined experimentally by monitoring the parallel energy of the slow ions leaving the plasma along the magnetic axis. The parallel ion energy is a measure of the plasma potential because the slow ions, born in the plasma, are pushed out along the magnetic field lines by the positive potential, thus gaining energy by an amount corresponding to the potential. We assume the perpendicular energy of these ions to be small compared with their final parallel energy.

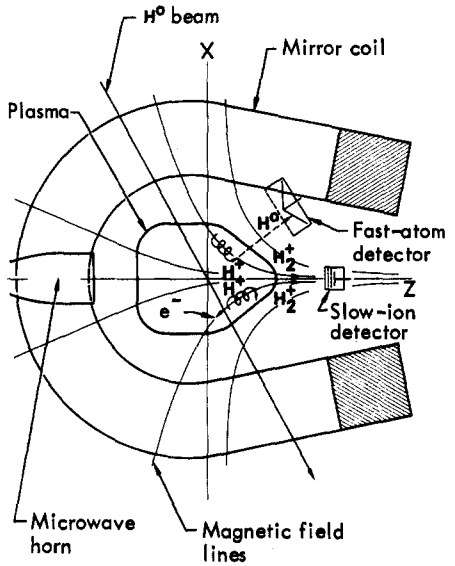

FIG. 3. Drawing showing location of detectors in relation to the plasma and the coil used to create the magnetic mirrors. The coil is wound in the shape of the seam on a baseball. The two main processes for producing slow ions are shown schematically.

These slow ions are produced mainly by two types of processes. The first is the charge exchange of the trapped fast ions on the background gas, shown sche-

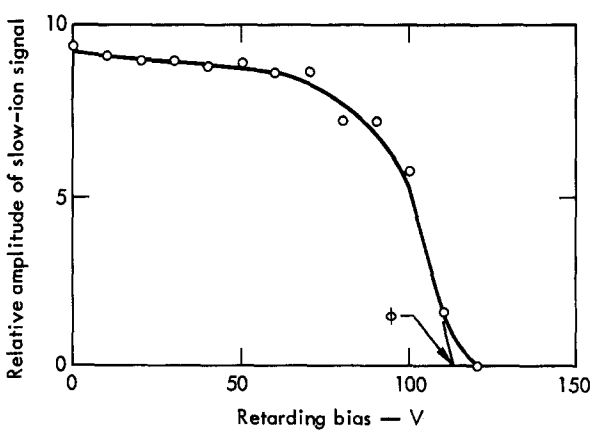

FIG. 4. Slow-ion amplitude versus retarding bias, as measured by the gridded slow-ion detector. The intercept labeled ϕ is considered the plasma potential.

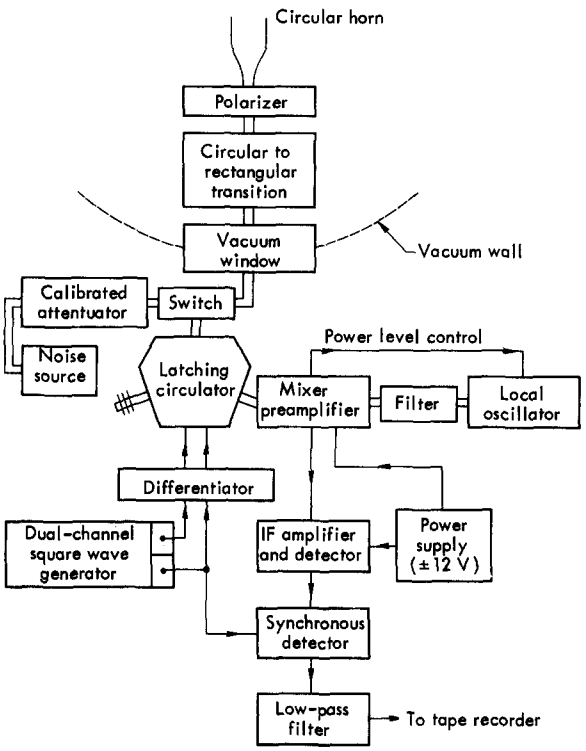

FIG. 5. Schematic diagram of the experimental apparatus for measuring electron temperature.

matically just above the center of Fig. 3. The second is ionization of the background gas, by either the trapped fast ions or the trapped electrons. Ionization by the ions is shown just below the center in Fig. 3. In both types of processes the production rate of slow ions is proportional to the trapped-particle density.

The slow-ion detector is a collector plate preceded by three grids (see Fig. 3). Voltages are applied to the grids to sort out ions from electrons and also to measure the maximum parallel energy of the ions (by determining the retarding bias needed to quench the ion signal).

The retarding bias is swept at a rate of about 10 Hz, resulting in many plots like that of Fig. 4 during each plasma containment time. At least two factors cause the decrease in slow-ion amplitude to be somewhat gradual. First, the slow ions reaching the detector are born at various positions in the plasma, thus originating over a range of potential values. Second, the shape of the plot may be influenced to some extent by the small spread of bias across the holes in the retarding grid, each of area 7.0×10^{-3} cm^2. This second effect is estimated to be relatively small, and will be neglected.

We approximate the maximum value of the potential in the plasma by the downward extension of the sharply falling portion of the retarding-bias plot, as shown in Fig. 4. In this manner we obtain intercepts whose values are quoted in Sec. IV as the plasma potential ϕ.

In Sec. IV we compare the decay time of the plasma potential, after the neutral beam is turned off, with the decay time of the trapped-ion density. We monitor ion density by observing the rate at which fast charge-exchange neutral particles leave the plasma. The fast-atom detector is a secondary-electron-emission type, positioned as shown in Fig. 3.

B. Electron Temperature Measurements

Measurements of the electron cyclotron radiation emitted from the plasma were made using a radiometer similar to that of Dicke.[19] For a tenuous plasma, the electron cyclotron radiation is proportional to the product of the electron density and the electron temperature.[20] Since measurements of the plasma density are available from other detectors, relative measurements of the electron temperature may easily be obtained from the intensity of the electron-cyclotron radiation.

Figure 5 is a schematic diagram of the apparatus used for the present measurements in the range 10.2–11.6 GHz. A circular horn 15 cm in diameter receives circularly polarized radiation from the plasma. A polarizer converts this circularly polarized radiation into linearly polarized radiation, preventing the loss of signal in the transition to rectangular wave guide. A manual switch permits radiation from either the plasma or a noise source to enter a latching circulator capable of switching rates up to 10 kHz. This device (with 20-dB isolation and 0.3-dB insertion loss) alternately passes or stops the incoming radiation, producing a square-wave modulation of the signal. (The "off" por-

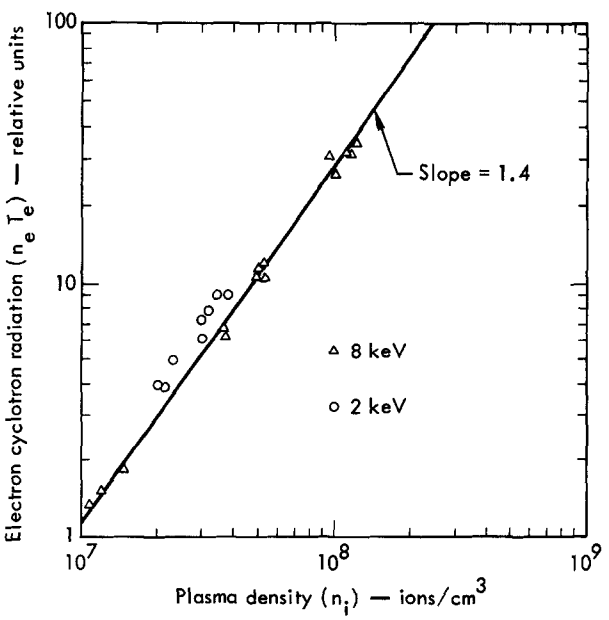

FIG. 6. Intensity of radiation emitted at the electron cyclotron frequency as a function of n_i, for hot-ion energies of 8 and 2 keV.

tion of the square wave corresponds to radiation from the matched load, which is at room temperature.)

The radiation then enters a balanced mixer preamplifier. The electrically tunable local oscillator has a frequency automatically tuned to track the electron cyclotron frequency in a selected portion of the plasma, in spite of unavoidable variations in the current of the confining-field magnet. The gain stability of the amplifying system is improved by feedback from the crystal current of the balanced mixer to control the output power from the local oscillator. Both sidebands of the mixer output are used. The signal then passes through an IF amplifier having a bandwidth of 40 MHz and a center frequency of 60 MHz. The plasma region sampled (neglecting Doppler broadening, etc.) thus is represented by the volumes in the "wall thickness" of two nested closed shells. The wall thickness of each shell corresponds to the 40-MHz bandwidth, and the unsampled volume between the shells corresponds to the 80-MHz separation of the inner edges of the two sidebands. Doppler broadening, which blurs the boundaries of the sampled volume, is assumed to have a negligible over-all effect since the radiation shifted into the accepted bands approximately equals that shifted out. The wide bandwidth of the receiver tends to iron out the effect of variations in the coupling of the horn antenna to the plasma which arise because of cavity resonances in the complicated vacuum chamber.

The detected output from the IF amplifier is modulated at the switching frequency of the latching circulator. The signal is fed into a narrow band ac amplifier and synchronous detector which is phase-locked to the same switching frequency. A low pass filter converts the output from the synchronous detector to a dc signal which is then recorded on magnetic tape.

In the present measurements, for which the plasma is tenuous, the electron cyclotron radiation is proportional to the product of the electron density and the electron temperature. According to Eq. (15), T_e is proportional to $(n_i/n_0)^{0.4}$. Therefore, the intensity of the radiation emitted is proportional to $n_i^{1.4}$. In practice, some variation in the background gas density could not be avoided; however, this dependence is eliminated by dividing the intensity of the emitted electron cyclotron radiation by $\tau_{cx}^{2/5}$, where τ_{cx} is the characteristic decay time due to charge exchange and is inversely proportional to n_0. Following this procedure, we obtain the results shown in Fig. 6 when the electron radiation is plotted as a function of n_i. The dependence on n_i for measurements made at ion energies of 8 and 2 keV is in good agreement with the $n_i^{1.4}$ dependence expected from theory. These results are discussed below at greater length.

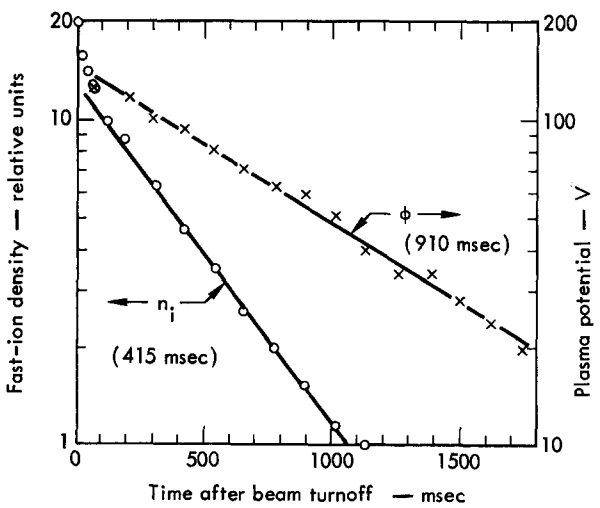

FIG. 7. Behavior of the plasma potential and fast-ion density during one plasma decay. Numbers in parentheses are characteristic decay time constants.

IV. COMPARISON OF THEORY AND EXPERIMENT

A. Equilibrium Case

In this section we compare the experimental results with predictions of the simple-model theory of Sec. II, which employs first-order differential equations. Comparison is also made between results of the simple-model theory and those of the Fokker–Planck equations. We concentrate here on the equilibrium situation, i.e., where changes in the plasma density are slow compared with the collisional relaxation time of the electrons.

The outstanding characteristic of the experimental data is that they agree with the easy-to-remember theoretical result that the plasma potential and electron temperature vary as $(n_i/n_0)^{2/5}$. This behavior as a function of the trapped-ion and background-gas densities was given by Eqs. (15) and (16), approximating the more complete theory represented by Eqs. (6) and (10).

We first discuss the results of the plasma-potential measurements. The experimental method for obtaining these data was presented in Sec. IIIA. Following beam turnoff, the plasma density may be represented by

$$n_i = n_{eq} \exp(-t/\tau_{cx}), \tag{18}$$

where n_{eq} is the plasma density at the time of beam turnoff and τ_{cx} is the characteristic charge-exchange decay time constant. By substituting Eq. (18) into the relationship $\phi \propto (n_i/n_0)^{2/5}$, one obtains the condition that the plasma potential decays with a time constant equal to $2.5\tau_{cx}$. This assumes quasiequilibrium conditions and a constant n_0. Figure 7 shows the experimental behavior of the plasma potential and the fast-proton density during one of our plasma decays. We observe that the potential decreases at a much slower rate after beam turnoff than the ion density, with the ratio of the time constants approaching the predicted value of 2.5. (These data, like the rest of the experimental plasma-

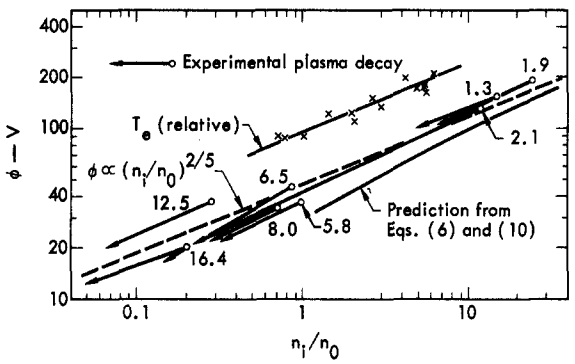

FIG. 8. Plasma potential and electron temperature vs n_i/n_0 from both experiment and theory. The numbers beside the circles give the background-gas densities for the individual decays in units of 10^7 molecules/cm^3. All the results here represent plasma-potential behavior except the upper data, which show relative T_e behavior.

potential results discussed here, were obtained at 15-keV injection energy.)

Several of these decays have been analyzed and the data summarized in Fig. 8. There we show results, both experimental and theoretical, of potential vs n_i/n_0. The circle at the right end of each individual experimental decay represents the earliest point on the decay after beam turnoff at which the plasma has settled down. After that, the fast-ion and plasma-potential decay times are about constant. We disregard the period directly after beam termination, during which the plasma potential often behaves erratically. The erratic behavior probably is due to the unstable condition of the plasma just before beam turnoff and to the nonequilibrium effect following beam turnoff. This latter effect will be discussed later.

The arrow starting at a given circle and pointing to the lower left shows the measured behavior of the potential during the rest of that plasma decay. The attached arrowhead is positioned at the end of the analyzed data. The numbers by the circles give the background-gas densities in units of 10^7 molecules/cm^3 for the various examples of plasma decay, assuming hydrogen molecules as the main constituent. These densities range over a factor of 12, from 1.3×10^7 to 1.6×10^8 cm^{-3}. The fast-proton densities represented by the data extend over a factor of 58, from 8.0×10^6 to 4.6×10^8 ions/cm^3. (All ion densities cited are peak densities.)

The slope of the dashed line in Fig. 8, arbitrarily normalized to fit the data, is that of the predicted $(n_i/n_0)^{2/5}$ variation. It is in agreement with the general trend of the experimental data. We will make a more quantitative comparison shortly.

Also shown in Fig. 8 are the results predicted by the more complete theory represented by Eqs. (6) and (10), which yield a magnitude as well as a slope. In these calculations we use 15 keV for the proton energy and 0.015 keV for E_0, the energy with which the electrons are born. Also, we use for $\overline{\sigma_e{}^e v_e}$ the value for electrons at energy $e\phi$ rather than at some other energy, such as kT_e. From these calculations, one again observes that the predicted slope is in approximate agreement with the data. One also notices that the predicted magnitude of the plasma potential lies close to the plotted experimental values. In general, the agreement between experiment and theory is good. It is better toward the lower left of the plot than might be expected, considering that the uncertainties both in theory and experiment become more dominant there.

We now examine the agreement between the data and theory more quantitatively. From the slope of each plasma decay in Fig. 8, we can calculate a value for the exponent in the power law relating the plasma potential and fast-ion density. The average for the eight experimental values is 0.45 ± 0.06, as compared to the basic predicted value of $\frac{2}{5}$ or 0.40. A value of 0.48 is obtained from the more refined calculation based on Eqs. (6) and (10).

The good agreement here may be somewhat fortuitous because of the various uncertainties involved, such as uncertainty about the composition of the background gas, uncertainties in measuring the experimental ion-density and plasma-potential decay characteristics, and approximations in the theory. Also, the equations were derived for the equilibrium situation, thus representing the plasma during decay only if the time-dependent effects are negligible. The period directly after beam turnoff is not included in these data, to minimize the effects of the nonequilibrium during this period (see Sec. IVB). Despite the uncertainties, the average of the data falls close to theoretical predictions.

In the results presented here, we have emphasized agreement of the data with the $n_i{}^{2/5}$ theoretical prediction. From Fig. 8, one can also note the predicted $n_0{}^{-2/5}$ variation. The data for the eight decays, although representing a factor-of-12 variation in n_0, still cluster around the predicted dashed slope. A variation with n_0 much different from the $-\frac{2}{5}$ power would not have given this result. Some of the observed data scatter may be due to variations in the background-gas composition, not considered in the calculation of n_0.

Also shown in Fig. 8 are measurements of the electron temperature (at 8 keV) taken by the technique in Sec. IIIB. This technique gives relative and not absolute values. The electron-temperature data are arbitrarily placed high on the plot, so as not to interfere with presentation of the plasma-potential data. Once again, the average slope, indicated by the straight-line fit to the data, is the predicted $(n_i/n_0)^{2/5}$ behavior, a further experimental verification of the theory.

We now turn to comparing the results of the simple differential-equation model with those of the Fokker–Planck equations. The Fokker–Planck results were obtained at 1 keV, so the comparison is made at a lower

energy than the 8–15-keV range discussed above. The Fokker–Planck calculations and analytical results are given in Fig. 9. Comparing the electron-temperature calculations from the analytical solutions with those from the Fokker–Planck equations shows reasonable agreement. The plasma-potential results in both cases, as expected, scale as $(n_i/n_0)^{2/5}$, although the absolute magnitudes are not in as good agreement as for the kT_e calculations. A difference of this magnitude is not unexpected, probably resulting from the use of average cross sections in the analytical calculations. In the Fokker–Planck equations, the more significant cross

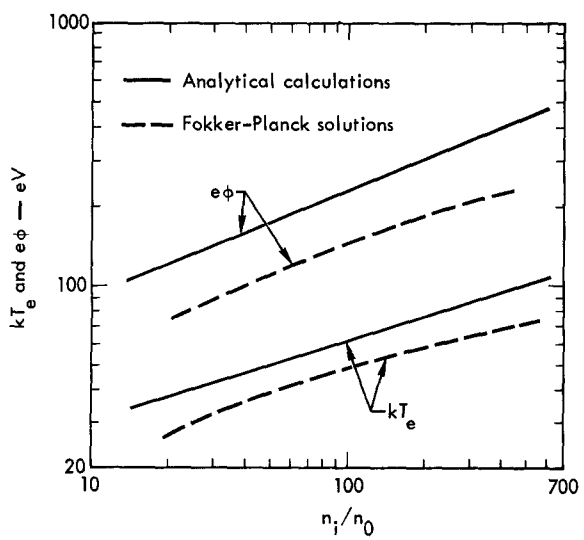

FIG. 9. Comparison of the analytical calculations of the electron temperature and plasma potential with the numerical solutions of the Fokker–Planck equations, for a 1-keV hot-ion plasma.

sections (e.g., σ_s^e, σ_s^i, and σ_{cx}) are treated correctly as a function of energy.

B. Nonequilibrium Case

Some important physical processes of interest in high-temperature plasmas are time-dependent or of a nonequilibrium nature. In this section we explain how solutions of the time-dependent Fokker–Planck equations are helpful in interpreting experimental data. We limit our discussion to a specific example, in which a changing electron temperature is a factor influencing the stability of an electrostatic "Harris-type" mode in the plasma.

The behavior of a 15-keV plasma produced by injection and trapping of energetic neutral atoms is shown in Fig. 10 under conditions of strong instability activity. The neutral atom beam is on for approximately 3 sec. During this time the plasma density builds up and becomes strongly unstable. This unstable behavior

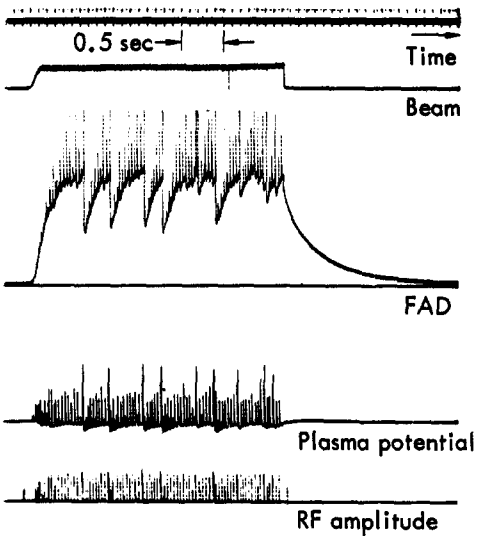

FIG. 10. Comparison of plasma density, plasma potential, and rf amplitude versus time, for a 15-keV hot-ion plasma. These measurements indicate that the plasma is stable during most of the decay following beam turnoff.

results in plasma losses correlated with rf activity and large excursions of the plasma potential. The plasma is observed to be stable over most of its decay following beam turnoff. The plasma-potential signal in Fig. 10 is not the slow-ion cutoff signal discussed elsewhere in this article. This electrostatic pickup signal results from the instability, and is much larger than the dc-potential signal.

In an earlier paper, it was suggested that the quiescent period between bursts, and also the stable decay,

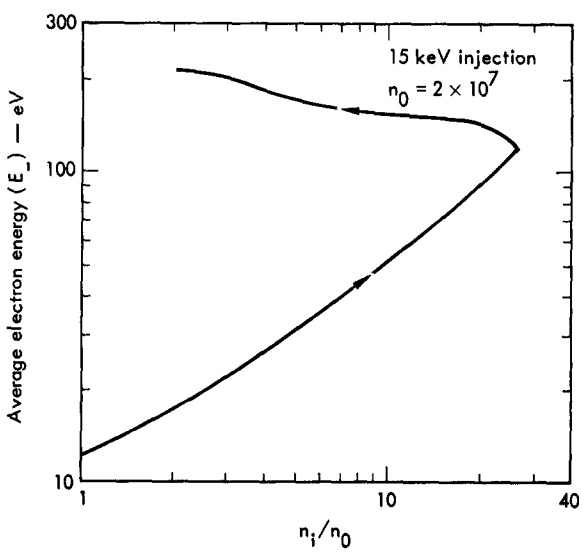

FIG. 11. Average electron energy E_- as a function of n_i/n_0 during plasma buildup to an equilibrium density of 5×10^8 ions/cm^3 and during the plasma decay following beam turnoff.

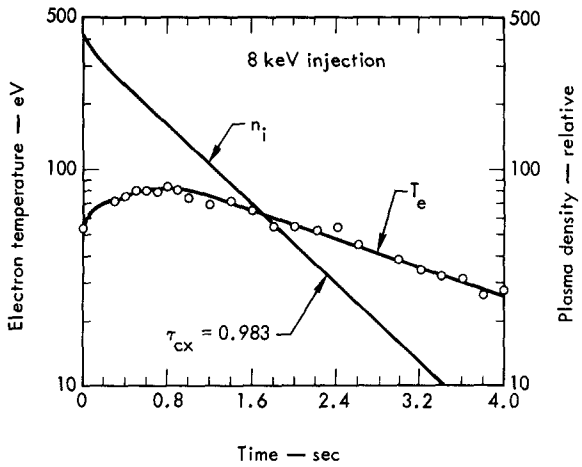

FIG. 12. Electron temperature and plasma density vs time during the decay of a 8-keV hot-ion plasma.

might be associated with a change in the electron distribution function.[21] Additional results now indicate that an increase in the electron temperature plays a significant role in stabilizing the plasma during the decay following beam turnoff. One example is the Fokker–Planck results displayed in Fig. 2. The parameters for these calculations were chosen to correspond to the experimental parameters of the plasma produced by the beam pulse of Fig. 10.

As exhibited by the Fokker–Planck calculations of Fig. 2, the average electron energy is seen to increase during the plasma decay following beam turnoff. The time-dependent or nonequilibrium nature of these calculations is clearly indicated by replotting the data from Fig. 2 in the form shown in Fig. 11. The lower curve gives the electron energy during buildup of the plasma density, and the upper curve gives the electron energy during the decay following beam turnoff. The electron energy is not just a function of the ratio n_i/n_0, as in the equilibrium case, but increases following beam turnoff and is significantly higher during plasma decay than during buildup.

An increasing electron temperature following beam turnoff is expected from a consideration of the simple heat balance equation

$$\frac{d}{dt}\left(\tfrac{3}{2}n_e k T_e\right) = \frac{3}{2}kT_e\frac{dn_e}{dt} + \frac{3}{2}n_e k\frac{dT_e}{dt}$$
$$= -\left[n_e^2(\overline{\sigma_s^e v_e})F(e\phi/kT_e)\right](e\phi) + n_e n_i G(W, T_e), \quad (19)$$

where $F(e\phi/kT_e)$ is defined in Sec. IIA and $G(W, T_e)$ is a function of the ion and electron energies. The first term on the right-hand side of Eq. (19) represents the rate at which electrons remove heat from the plasma by escaping over the potential barrier; the second term is the rate at which electrons gain energy by collisions with the ions. In this equation we neglect the energy with which the electrons are born. At equilibrium, the left side of Eq. (19) must be equal to zero since neither n_e or T_e are changing with time; therefore, the right side also is zero. Also, the right side is zero immediately after beam turnoff, and remains approximately zero during the initial decay since both the ion–electron transfer rate and the electron loss rate are binary processes. Therefore, the left side is still zero following beam turnoff, and we have

$$\frac{dT_e}{dt} = -\frac{T_e}{n_e}\frac{dn_e}{dt} = \frac{T_e}{\tau_{cx}}, \quad (20)$$

where τ_{cx} is the characteristic charge-exchange time. The electron temperature thus increases temporarily after beam turnoff on a time scale τ_{cx}.

We also have experimental measurements showing an increase in electron temperature following beam turnoff. Both the plasma density n_i and the electron temperature T_e are plotted in Fig. 12 as a function of time following beam turnoff. The electron temperature was obtained from microwave measurements of the emitted radiation at the electron cyclotron frequency, as described in Sec. III. The measured value of T_e was normalized to a calculated value of T_e at the time of beam turnoff. Figure 12 shows that T_e does not increase indefinitely, but begins to decrease after a time following beam turnoff comparable to τ_{cx}.

Further experimental evidence for the nonequilibrium condition of the plasma directly after beam turnoff is the temporary increase in electrostatic potential frequently observed at that time. Here again, the parallel

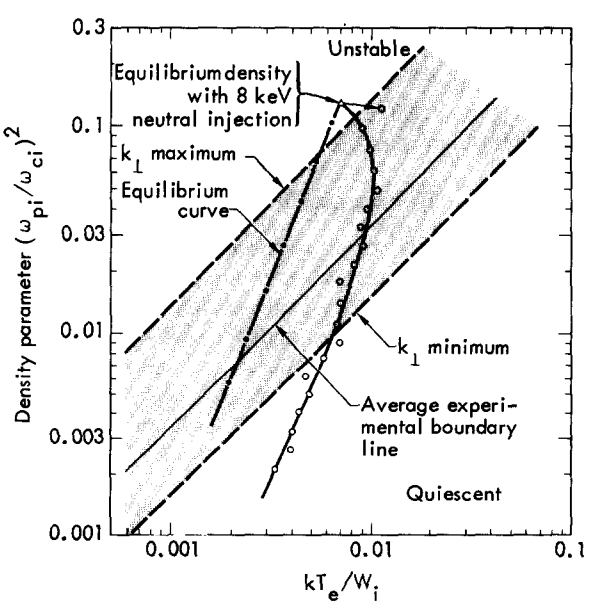

FIG. 13. Threshold for instability in terms of the density parameter $(\omega_{pi}/\omega_{ci})^2$ vs kT_e/W_i.

energy of the slow ions is the measure of potential. As in the case of T_e, the transient increase in potential is followed by the customary gradual decay.

In Fig. 13 we replot the experimental data of Fig. 12 and make a comparison with instability-threshold data. The solid straight line of Fig. 13 gives the average instability threshold for the ion-cyclotron instability observed in the Livermore neutral-injection experiment in terms of the density parameter $\epsilon=(\omega_{pi}/\omega_{ci})^2$ as a function of the ratio kT_e/W_i, where W_i is the ion energy.[22] This instability-threshold line is obtained by replotting the average experimental boundary line given in Fig. 2a of Ref. 22 as a function of kT_e/W_i instead of $e\phi_M/W_i$. A theoretical value for the ratio $kT_e/e\phi_M$ is used in making this transformation. Individual threshold values are found to deviate from the average experimental boundary line by an amount clearly outside the error assignments. The perpendicular component of the propagation vector $k_\perp$ is shown to be quantized, with deviations from the average boundary line resulting from $k_\perp$ taking on different quantized values. The dashed lines of Fig. 13 correspond to the maximum and minimum values observed for $k_\perp$. We have used the same ratio of $kT_e/e\phi_M$ in these transformations as in the transformation of the average threshold line.

The triangle at the top in Fig. 13 shows the equilibrium density attained for 8-keV neutral injection. The achieved density lies above the threshold for the instability. Following an instability burst, the electron temperature increases; the point characterizing the plasma (Fig. 13) moves to the right from its equilibrium position toward the average stable threshold line, as indicated by the arrow. After the instability activity, the temperature relaxes back toward its equilibrium value until the plasma again becomes unstable. Following beam turnoff, the plasma then decays, following the curved path indicated on Fig. 13 and reaching the average instability-threshold line at $\epsilon=0.032$. If the electron temperature varied as expected for equilibrium conditions, i.e., T_e proportional to $(n^+)^{2/5}$, the plasma would decay following a straight line of slope 2.5 and reach the average instability-threshold line at $\epsilon=0.0074$.

The evidence at this time indicates that the changing electron distribution is a significant factor in determining the stability of the plasma between bursts and during the decay following beam turnoff. The experimental curve in Fig. 13 shows how the increasing electron temperature after beam turnoff enables the plasma quickly to reach the stable region. The electrons may play more of a role in determining stability than indicated by the comparison in Fig. 13, since the criterion for determining stability during decay cannot be the same as that applied to determine the threshold curve. The threshold curve was determined by requiring a total absence of instability bursts for approximately three charge-exchange times, while during decay the plasma would have reached the stable region in a time short compared with $3\tau_{cx}$.

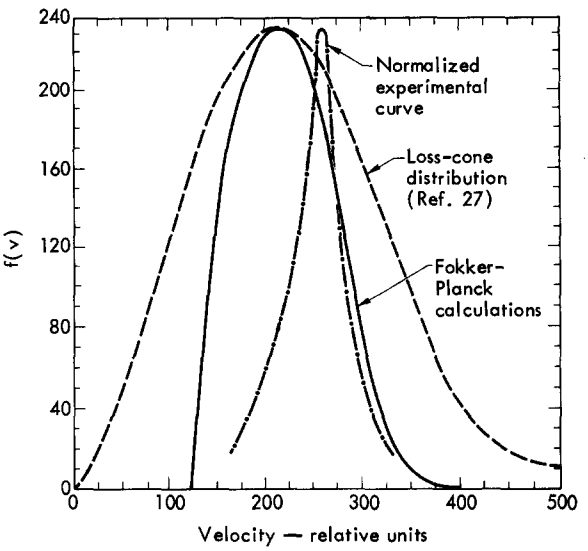

FIG. 14. Comparison of various ion distributions for a mirror ratio of 2. The Fokker–Planck calculations contain a source and charge-exchange loss term.

V. COLLISIONAL BROADENING OF THE ION DISTRIBUTION FUNCTION

Plasmas formed in neutral injection experiments by the trapping of neutral atoms in the energy range 5–20 keV have been subject to velocity-space instabilities resulting from the nearly monoenergetic and highly anisotropic nature of the ion distribution function.[23–25] An important objective of the Livermore neutral-injection experiment Alice is to reduce the injection energy to a sufficiently low value such that Coulomb collisions broaden the ion distribution function, thereby reducing the driving terms of the instability. A significant broadening of the distribution function is predicted when the charge-exchange time τ_{cx} equals the Coulomb scattering time, τ_s.[26] This equality has been used to determine the required beam and vacuum conditions.

Fokker–Planck calculations appropriate to low-energy injection were undertaken to determine the ion and electron distribution functions more accurately in the presence of the source, charge-exchange losses, and scattering losses. The various input parameters correspond to the injection and trapping of neutral hydrogen atoms having an energy of 1 keV. The calculations reported here do not include the effect of charge exchange between protons and beam atoms. This process, which is negligible for the present calculations, tends to sharpen the trapped distribution.

Figure 14 compares the various ion distribution functions. The dashed curve is the analytical loss-cone distri-

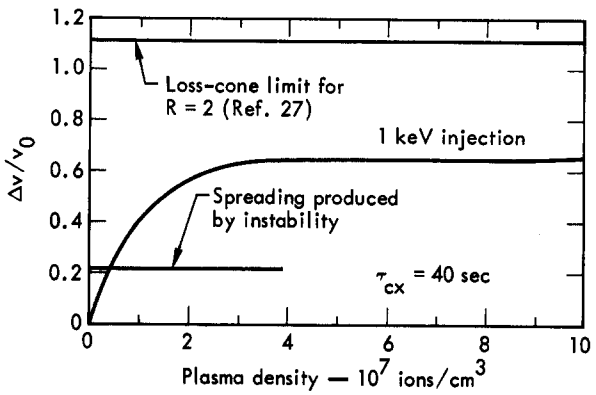

FIG. 15. Relative width of ion distribution versus equilibrium ion density.

bution for a mirror ratio of 2 as obtained by BenDaniel and Allis.[27] The equilibrium ion distribution from the Fokker–Planck calculations containing a source and both charge-exchange and scattering losses is shown by a solid line. Using the formula of Post and Damm,[28] we determined the input parameters for the Fokker–Planck problem by the condition that $\tau_s = \tau_{cx}$. The charge-exchange time τ_{cx} was chosen to be 40 sec and independent of energy. The mirror ratio was 2. The Fokker–Planck results gave a large energy spread and an end-loss rate three times greater than would be expected from the analytical expression for the scattering cross section.

The experimental curve in Fig. 14 indicates the relative spreading of the distribution function in the presence of the instability. This curve was obtained at 15 keV; the velocity is scaled down such that the peak of the distribution occurs at a velocity corresponding to 1 keV. At 1 keV, a significant loss of ion energy to the electrons occurs, resulting in a shift of the distribution peak to a lower velocity (as indicated by the other curves).

The Fokker–Planck calculations of Fig. 14 correspond to an equilibrium ion density of 10^8 ions/cm^3. At low densities, both the equilibrium ion density and the width of the ion distribution function increase as the injected beam current is increased. As a measure of the relative width of the distribution, we use $\Delta v/v_0$, the full-width at half-maximum divided by the velocity at the peak of the distribution. Figure 15 shows how this quantity varies as a function of the equilibrium ion density. Both the loss-cone limit and the spreading produced by a velocity-space instability in the Livermore neutral-injection experiment are indicated on Fig. 15 for comparison. At 1 keV, the relative spreading produced by collisions should be at least as large as the relative instability spreading observed at the higher energies, if the charge-exchange time is as large as 40 sec. (Diagnostics are not available at present for making this measurement.)

VI. CONCLUDING REMARKS

We have described collisional processes in high-temperature plasmas in terms of a self-consistent theory which relates basic plasma parameters such as the electron temperature, ion energy, and plasma potential to the plasma density. A simple model describing plasmas in quasiequilibrium, for which analytical solutions may be obtained, has been shown to give the correct relationship between many plasma parameters. Experimental measurements of the plasma potential ϕ and the electron temperature T_e are in good agreement with this simple model. Both T_e and ϕ are found to scale with the $\frac{2}{5}$ power of the ratio n_i/n_0, as expected.

Fokker–Planck results agree with the simple theory, and the calculations follow the same $\frac{2}{5}$ scaling law under equilibrium conditions. The Fokker–Planck equations were solved to study the nonequilibrium nature of the electron temperature and plasma potential during plasma decay. These calculations indicate that the initial increase in electron temperature following beam turnoff is a significant factor in the stability of the plasma during decay. Electron-temperature measurements have been presented which have the same time-dependent behavior during plasma decay as predicted by the Fokker–Planck calculations.

Numerical solutions of the Fokker–Planck equations have been used to determine the plasma density necessary to approach a loss-cone distribution for the ions. These results give a larger energy spread and end loss than indicated by earlier calculations.[28] This difference is partially explained by degradation of the ion energy, which results from collisions with the electrons. The earlier calculations, in which the ion energy was considered constant, did not take into account this effect.

ACKNOWLEDGMENTS

The authors are grateful to T. K. Fowler and R. F. Post for helpful discussions, and acknowledge the help of Shirley Rompel in writing the numerical program to solve the Fokker–Planck equations.

This work was performed under the auspices of the United States Atomic Energy Commission.

APPENDIX

As discussed in Sec. IIB, we have modified the Fokker–Planck equation to include source and loss terms. The collisional loss rate may be written in terms of the distribution function $f_a(v, t)$ for particles of type "a." We use the form given by BenDaniel and Allis,[6] i.e.,

$$\frac{dn_a}{dt} = -(4\pi)^2 \int_0^\infty f_a(v,t)v^2 \times \left(\sum_b \int_0^\infty k_a(v,v')f_b(v',t)v'^2\,dv'\right)dv, \quad \text{(A1)}$$

where

$$k_a(v, v') = \Gamma_a(\Lambda_a/2v^3) \begin{cases} 1-\frac{1}{3}(v'^2/v^2) & v \geq v', \\ \frac{2}{3}(v/v') & v \leq v', \end{cases} \quad \text{(A2)}$$

and

$$\Lambda_a = (\log_{10} R_a^{\text{eff}})^{-1}. \quad \text{(A3)}$$

The effective mirror ratio, R_a^{eff}, is given by

$$R_a^{\text{eff}} = R[1 \pm (m_e/m_a)(v_c^2/v^2)]^{-1}, \quad \text{(A4)}$$

except $R_a^{\text{eff}} = 1$ when Eq. (A4) gives values of R_a^{eff} less than unity and greater than zero; $R_a^{\text{eff}} = \infty$ for negative values of R_a^{eff}. In Eq. (A4), R is the true mirror ratio; the sign is chosen to correspond to the sign of the particle being scattered.

The velocity v_c is determined by the condition that the electron kinetic energy is just equal to the plasma potential, i.e.,

$$e\phi = \tfrac{1}{2} m_e v_e^2. \quad \text{(A5)}$$

We define the constant Γ_a by the equation

$$\Gamma_a \equiv (4\pi e^4/m_a^2) \ln D. \quad \text{(A6)}$$

The quantity D is the ratio of the Debye length to the classical distance of closest approach. We consider electrons and ions of $Z = 1$. We introduce

$$f_a = (4\pi v_0^3/K_a) f_a,$$

where K_a is determined from the equation

$$n_a(0) = K_a \int_0^\infty f_a(x, 0) x^2 \, dx, \quad \text{(A7)}$$

where $x = v/v_0$. The constant v_0 is a characteristic velocity. We introduce the dimensionless variable τ, where $\tau = (\frac{1}{2}\Gamma_e K_e/v_0^3)t$, and define functionals

$$M(f_a) = \int_x^\infty f_a(y, \tau) y \, dy, \quad \text{(A8)}$$

$$N(f_a) = \int_0^x f_a(y, \tau) y^2 \, dy, \quad \text{(A9)}$$

and

$$E(f_a) = \int_0^x f_a(y, \tau) y^4 \, dy. \quad \text{(A10)}$$

In terms of these new variables, the Fokker–Planck equation for the distribution functions becomes[15]

$$\frac{\partial f_a}{\partial \tau} = A \frac{\partial^2 f_a}{\partial x^2} + B \frac{\partial f_a}{\partial x} + C f_a + D, \quad \text{(A11)}$$

where

$$A = \tfrac{2}{3} \sum_b K_b/K_e[(1/x^3)E(f_b) + M(f_b)],$$

$$B = (4/3x) \sum_b K_b/K_e[(3/2x)(m_a/m_b)N(f_b) - (1/2x^3)E(f_b) + M(f_b)],$$

and

$$C = 2\left(\frac{m_e}{m_a}\right)^2 \sum_b \left(\frac{m_a}{m_b}\right)\left(\frac{K_b}{K_e}\right) f_b - \frac{2\Lambda_a}{3x^2} \sum_b \frac{K_b}{K_e} \times \left(\frac{3}{2x} N(f_b) - \frac{1}{2x^3} E(f_b) + M(f_b)\right) - H_a(x, \tau).$$

The term $D(x, \tau)$ describes the time-dependent sources and $H_a(x, \tau)$ is the charge-exchange loss term, which is zero for electrons.

At any time step we can determine the number density and average energy of each type of particle. Let $I_2^a(\tau)$ and $I_4^a(\tau)$ be the second and fourth moments of the distribution functions, i.e.,

$$I_2^a(\tau) = \int_0^\infty f_a(x, \tau) x^2 \, dx, \quad \text{(A12)}$$

$$I_4^a(\tau) = \int_0^\infty f_a(x, \tau) x^4 \, dx. \quad \text{(A13)}$$

The number density is given by

$$n_a(\tau) = K_a I_2^a(\tau), \quad \text{(A14)}$$

and the mean energy is given by

$$E_a(\tau) = \tfrac{3}{2} k T_a = \tfrac{1}{2} m_a v_0^2 [I_4^a(\tau)/I_2^a(\tau)]. \quad \text{(A15)}$$

We assume that the injected particles have a velocity distribution defined by $S_a(x)$. The source terms $D(x, \tau)$ are given by

$$D(x, \tau) = S_a(x) \left(\frac{t}{\tau}\right) \frac{1}{K_a N(S_a)} \left(\frac{dn_a}{dt}\right), \quad \text{(A16)}$$

where (dn_a/dt) is the trapping rate for particles of type "a." We can include up to 10 sources of the type given by Eq. (A16), corresponding to multiple beam injection at different energies.

In the above discussion of source terms, the (σv) terms were treated as constants; however, the cross sections have a velocity dependence determined by experimental measurements. We have polynomial descriptions for these functions so the terms $\sigma v n(\tau)$ can be replaced by integrals involving the distributions.

The critical velocity x_c is determined by the following procedure. At every time step $n_e(\tau)$ and $n_i(\tau)$ are computed, and the difference $| n_i(\tau) - n_e(\tau) |$ is also computed. Since we wish to keep $n_e(\tau) \cong n_i(\tau)$, the above difference is compared to a pre-assigned small number. If the difference exceeds this number, then x_c is increased by an amount Δx_c if $n_i(\tau) - n_e(\tau)$ is positive, or decreased by an amount Δx_c if $n_i(\tau) - n_e(\tau)$ is negative. The time step is then repeated. This process is repeated until $| n_i(\tau) - n_e(\tau) |$ is sufficiently small; the calculation is then continued.

The coupled nonlinear partial differential equations for the functions $f_a(v, t)$ are solved numerically using

finite-difference methods. The equations are not linearized, i.e., the coefficients involving moments of the distribution functions are computed at each time step. An implicit difference scheme is used, that is, the velocity derivatives are replaced by difference quotients taken at the new time step, while the coefficients are evaluated by use of the distribution function of the previous time step and then extrapolated. The scheme is numerically stable in practice, with no restriction on the time step. This is an essential part of the calculations because as the electron temperature increases, the transfer rate decreases; the time step Δt therefore must be increased continually for the calculation to progress toward equilibrium in a sensible manner. A more detailed description of this method for obtaining numerical solutions is given in Ref. 15.

* Present address: Department of Physics and Astronomy, Brigham Young University, Provo, Utah 84601.

[1] S. Chandrasekhar, *Principle of Stellar Dynamics* (University of Chicago Press, Chicago, Ill., 1942), p. 67.
[2] L. Spitzer, Jr., *Physics of Fully Ionized Gases* (Interscience, New York, 1956), p. 132.
[3] A. N. Kaufman, in U.S. Atomic Energy Report No. TID-7520, Vol. 2, p. 387.
[4] R. F. Post, Phys. Fluids **4**, 902 (1961).
[5] D. J. BenDaniel, Plasma Phys. **3**, 235 (1961).
[6] D. J. BenDaniel and W. P. Allis, Plasma Phys. **4**, 31 (1962); **4**, 79 (1962).
[7] J. Killeen and K. D. Marx, Methods Comput. Phys. **9**, 422 (1969).
[8] A. H. Futch, Jr., W. Heckrotte, C. C. Damm, J. Killeen, and L. E. Mish, Phys. Fluids **5**, 1277 (1962).
[9] M. N. Rosenbluth, W. M. MacDonald, and D. L. Judd, Phys. Rev. **107**, 1 (1957).
[10] G. F. Bing, D. L. Judd, W. M. MacDonald, and M. N. Rosenbluth, in U.S. Atomic Energy Report No. TID-7503.
[11] A. Garren, R. J. Riddell, L. Smith, G. Bing, L. R. Henrich, T. G. Northrop, and J. E. Roberts, in *Proceedings of the Second International Conference on the Peaceful Uses of Atomic Energy* (United Nations, Geneva, 1958), Vol. 31, p. 65.
[12] J. E. Roberts and M. L. Carr, Lawrence Radiation Laboratory, University of California, Livermore, Report UCRL-5651-T(1960).
[13] T. K. Fowler and M. Rankin, Plasma Phys. **4**, 311 (1962).
[14] G. F. Bing and J. E. Roberts, Phys. Fluids **4**, 1039 (1961).
[15] J. Killeen and A. H. Futch, J. Comput. Phys. **2**, 236 (1968).
[16] J. H. Foote, A. H. Futch, and C. C. Damm, Bull. Am. Phys. Soc. **13**, 1520 (1968).
[17] G. Hamilton (private communication).
[18] R. F. Post, Rev. Mod. Phys. **28**, 338 (1956).
[19] R. H. Dicke, Rev. Sci. Instr. **17**, 268 (1946).
[20] M. A. Heald and C. B. Wharton, *Plasma Diagnostics with Microwaves* (Wiley, New York, 1965), p. 273.
[21] A. H. Futch, C. C. Damm, J. H. Foote, and R. F. Post, Bull. Am. Phys. Soc. **13**, 1520 (1968).
[22] C. C. Damm, J. H. Foote, A. H. Futch, Jr., A. L. Hunt, K. Moses, R. F. Post, and J. B. Taylor, Phys. Rev. Letters **24**, 495 (1970).
[23] C. C. Damm, J. H. Foote, A. H. Futch, A. L. Gardner, and R. F. Post, Phys. Rev. Letters **13**, 464 (1964).
[24] A. H. Futch, Jr., C. C. Damm, J. H. Foote, R. Freis, F. J. Gordon, A. L. Hunt, J. Killeen, K. G. Moses, R. F. Post, and J. F. Steinhaus, in *Plasma Physics and Controlled Nuclear Fusion Research* (International Atomic Energy Agency, Vienna, 1966), Vol. II, p. 3.
[25] L. C. Kuo, E. G. Murphy, M. Petravic, and D. R. Sweetman, Phys. Fluids **7**, 988 (1964).
[26] R. F. Post and C. C. Damm (private communication).
[27] D. J. BenDaniel and W. P. Allis, Plasma Phys. **4**, 31 (1962).
[28] R. F. Post and C. C. Damm, Lawrence Radiation Laboratory, University of California, Livermore, Report UCID-15038 (1966).